ADVANCED MATERIALS
www.advmat.de

Buoyancy-Driven Gradients for Biomaterial Fabrication and Tissue Engineering

Chunching Li, Liliang Ouyang, Isaac J. Pence, Axel C. Moore, Yiyang Lin, Charles W. Winter, James P. K. Armstrong, and Molly M. Stevens**

The controlled fabrication of gradient materials is becoming increasingly important as the next generation of tissue engineering seeks to produce inhomogeneous constructs with physiological complexity. Current strategies for fabricating gradient materials can require highly specialized materials or equipment and cannot be generally applied to the wide range of systems used for tissue engineering. Here, the fundamental physical principle of buoyancy is exploited as a generalized approach for generating materials bearing well-defined compositional, mechanical, or biochemical gradients. Gradient formation is demonstrated across a range of different materials (e.g., polymers and hydrogels) and cargos (e.g., liposomes, nanoparticles, extracellular vesicles, macromolecules, and small molecules). As well as providing versatility, this buoyancy-driven gradient approach also offers speed (<1 min) and simplicity (a single injection) using standard laboratory apparatus. Moreover, this technique is readily applied to a major target in complex tissue engineering: the osteochondral interface. A bone morphogenetic protein 2 gradient, presented across a gelatin methacryloyl hydrogel laden with human mesenchymal stem cells, is used to locally stimulate osteogenesis and mineralization in order to produce integrated osteochondral tissue constructs. The versatility and accessibility of this fabrication platform should ensure widespread applicability and provide opportunities to generate other gradient materials or interfacial tissues.

In nature, gradients play an essential role in guiding the function of a wide range of tissues, including tendon, cartilage, and the central nervous system.[1–4] Strategies that seek to engineer tissues in vitro must strive to recreate these natural gradients in order to produce fully functional grafts or physiologically relevant models. In doing so, one must consider the numerous gradients present in native tissue, including transitions in biochemical composition (e.g., extracellular matrix and soluble growth factors) and physical environment (e.g., stiffness and topography). These transitions play a major role in defining the formation of cellular gradients by spatially regulating the morphology, behavior, and differentiation of local cells.[5–8] Accordingly, intensive research effort has been invested in designing materials with well-defined gradients. For instance, material gradients have been fabricated using multichannel microfluidic devices or 3D printing.[9–11] However, these approaches require specialist apparatus and are usually restricted by certain material parameters, such as viscosity or gelation kinetics. Approaches such as photopatterning and magnetic field alignment have also been used to generate gradients; however, these remote field strategies require even more specific material properties (photoresponsivity and magnetic susceptibility).[12,13] Indeed, a generalized method that can be universally applied to different systems has thus far remained elusive.

In this work, we sought to employ a more universal physical principle that could be applied broadly across different material systems. Specifically, we investigated whether we could fabricate material transitions using buoyancy, the upward force generated on materials immersed in a denser fluid phase.[14] Buoyancy is commonly used to stabilize the formation of sucrose gradients used for the fractionation of cells and organelles.[15,16] This approach has been extended to nanoparticle separation using density-graded organic solvents.[17] There are, however, only a limited number of examples in which buoyancy has been used to fabricate gradient materials. For example, Parameswaran and Shukla described a system in which cenospheres (hollow silica–alumina microparticles) were allowed to rise to the top of a polyester resin and then immobilized in a solid matrix using a 48 h curing process. This yielded a polymeric material with a graded volume fraction of cenospheres, and a corresponding gradient of compressive and tensile properties.[18] Similarly, Beals and Thompson showed that a gas injected into a molten aluminum alloy could be dispersed into small particulate-stabilized bubbles upon mixing. These bubbles formed a liquid foam at the top of the melt, which was subsequently cooled to

C. Li, L. Ouyang, I. J. Pence, A. C. Moore, Y. Lin, C. W. Winter, J. P. K. Armstrong, M. M. Stevens
Department of Materials
Department of Bioengineering and Institute of Biomedical Engineering
Imperial College London
Prince Consort Road, London SW7 2AZ, UK
E-mail: james.armstrong@imperial.ac.uk; m.stevens@imperial.ac.uk

The ORCID identification number(s) for the author(s) of this article can be found under https://doi.org/10.1002/adma.201900291.

DOI: 10.1002/adma.201900291

form a metallic structure with a gradient of porosity.[19] However, these examples are highly specific with a focus on solid materials for industrial applications. To the best of our knowledge, there has been no report of any versatile methodology using buoyancy in gradient material fabrication, nor any examples in which buoyancy-driven gradients have been applied to the field of complex tissue engineering.

To this end, we sought to develop a generalized buoyancy-driven approach for casting gradients that could be applied to real-world tissue engineering applications. Here we show that a single injection event of one fluid material into another is sufficient to generate material transitions that can be preserved by subsequent gelation or polymerization. Moreover, we were able to fabricate materials exhibiting either a sharp transition or a smooth gradient by systematically varying the material characteristics and injection parameters. We used this platform to cast gradients in several different materials (gelatin methacryloyl, gellan gum, agarose, and acrylate polymers) and generated tunable transitions in composition, biochemical profile, and compressive stiffness. We also demonstrated that several cargo species could be incorporated in gradient form, including inorganic nanoparticles, liposomes, cell-derived extracellular vesicles, macromolecules, and proteins. We applied this method to cast bone morphogenetic protein 2 (BMP-2) gradients for the in vitro engineering of osteochondral tissue constructs.[20] In this system, the encapsulated BMP-2 was slowly released over 28 d of tissue engineering to locally stimulate osteogenesis of human mesenchymal stem cells and produce osteochondral tissue bearing a defined mineral cap. The versatility and simplicity of this gradient casting platform should enable a range of applications in complex material fabrication and interfacial tissue engineering.

In order to rapidly cast different material gradients, we sought to develop and optimize a controlled two-component mixing system. Specifically, we used a commercially available electronic autopipette to introduce one material at a defined rate into another static base material. The two phases were allowed time to establish a gradient, which could then be preserved by triggering a polymerization or gelation process. This system only required two liquid phases that were miscible and curable, as well as a sufficient density difference to enable buoyancy-driven gradient formation (**Figure 1**A). This can be illustrated using the relatively simple case of 0.2 and 1% (w/v) agarose in the injection phase and base layer, respectively (Figure S1, Supporting Information). However, in scenarios where the density difference between the two phases was too small to create sufficient buoyancy, we used a third component to increase the density of the base layer relative to the injection phase. Using this approach, we were able to form smooth gradients using 1% (w/v) fluorescently tagged agarose and 1% (w/v) unlabeled agarose by adding 5% (w/v) sucrose to the base layer. Moreover, gradients could be rapidly established in 10 s, with the resulting structure remaining stable for at least 30 min post injection (Figure 1B; Figure S2 and Video S1, Supporting Information). This provided us with an ample window of opportunity to solidify the material and preserve the gradient, in this case, by cooling the system below the gelation temperature of agarose.

To characterize this system and elucidate the mechanism behind gradient formation, we analyzed the composition of the hydrogel along the longitudinal axis. We divided the hydrogels

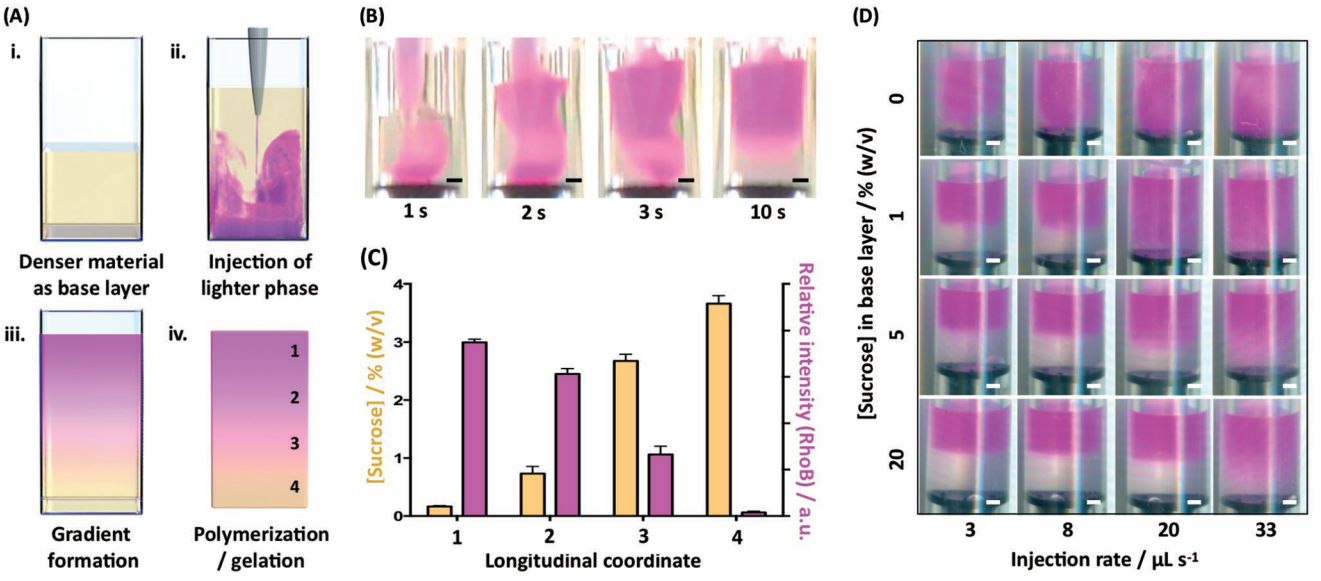

Figure 1. Buoyancy-driven gradient casting. A) Schematic showing the steps of gradient formation: i) a base layer (yellow) is added to a mold, ii) the injection phase (purple) is introduced during a single injection at a controlled rate, iii) the system is allowed to equilibrate and form a material gradient, and iv) the gradient is preserved by gelling or polymerizing the material. B) An example of gradient formation using 1% (w/v) agarose tagged with rhodamine B (pink) injected at a rate of 20 µL s^{-1} into a base layer of 1% (w/v) agarose supplemented with 5% (w/v) sucrose as a density modifier. An observable gradient can be established within 10 s. C) Immediately after gelation, a gradient hydrogel was equally divided into four transverse sections from the top to the bottom of the hydrogel (1–4). These sections were assayed for sucrose (yellow bars) and agarose tagged with rhodamine (RhoB, pink bars), which showed a clear inverse correlation. Data shown as mean ± S.D., $n = 3$. D) The gradient pattern could be tuned by varying the injection rate and concentration of sucrose in the base layer. For measured densities, see Figure S4 in the Supporting Information. Scale bars = 1 mm.

into four transverse sections, which we analyzed using an enzymatic assay for sucrose and fluorescence spectroscopy for dye-labeled agarose (Figure 1C). These measurements revealed a sucrose gradient within the hydrogel that was inversely associated with the injected dye-labeled agarose. These results suggest that sucrose must retain attractive intermolecular interactions with the base layer agarose during the fluid-mixing process. These interactions prevent the base layer from completely equilibrating with the injection phase, thus retaining longitudinal density differences capable of supporting buoyancy-driven gradient formation. It should also be noted that sucrose, as a small molecule, could be readily removed by washing the agarose hydrogel in phosphate buffered saline (PBS) (Figure S3, Supporting Information). In this sense, sucrose can be considered as a temporary density modifier that can template the gradient formation process. Moreover, we observed that systematic variation of different parameters could be used to control the final profile of the material gradient. Using the same agarose–sucrose system, we showed that different combinations of injection rate and density difference could be used to fabricate a range of transitions, from sharp layers to smooth gradients (Figure 1D; Figure S4, Supporting Information). Indeed, small differences in density from the doped sucrose ($\Delta\rho$ = 0.02 g mL^{-1}) were enough to drive gradient formation, while no clear structural transitions could be formed without addition of sucrose to the agarose base layer.

Unlike the majority of gradient fabrication strategies, which are only applicable to certain materials or cargos, our buoyancy platform could be widely applied across different systems. To illustrate this versatility, we demonstrated seven distinct examples of buoyancy-driven gradient formation (Table S1, Supporting Information). First, we generated gradients in solid polymers using two miscible monomers bearing a slight difference in material density, *N*,*N*-dimethylacrylamide (ρ = 0.96 g mL^{-1}) and lauryl methacrylate (ρ = 0.87 g mL^{-1}), together with poly(ethylene glycol) dimethacrylate as a crosslinker. Inclusion of photoinitiator allowed us to trigger photopolymerization after establishment of the monomer gradient. We visualized this transition by adding rhodamine B dye, which is soluble in *N*,*N*-dimethylacrylamide but not in lauryl methacrylate (**Figure 2**A). We further characterized this transition using Raman spectroscopy based on the distinct signature of the two polymers (Figure 2A; Figure S5, Supporting Information). Next, we used our buoyancy platform to pattern defined stiffness transitions into 1% and 1.5% (w/v) gellan gum hydrogels, using 5% (w/v) sucrose as a density modifier. We measured the contact modulus along the longitudinal axis using a spherical indenter, which revealed the different stiffness transitions that we could achieve by varying the injection rate (Figure 2B). As well as creating transitions in the bulk material structure, we also used our buoyancy platform to fabricate materials bearing gradients of encapsulated

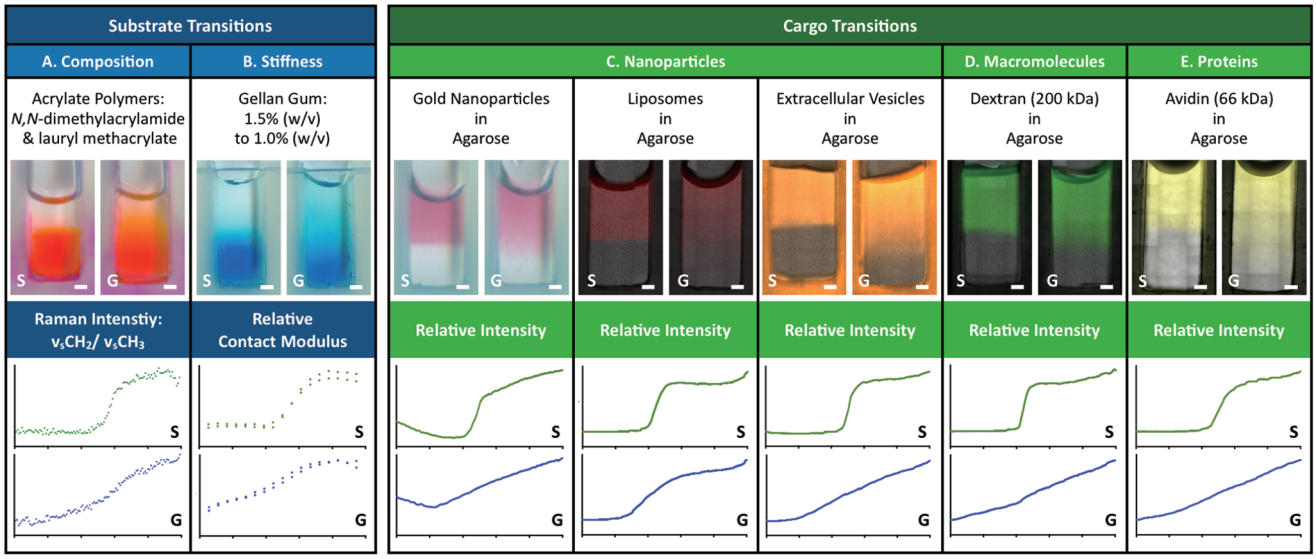

Figure 2. Versatility of buoyancy-driven gradient formation. For all fabricated materials, we generated sharp transitions (S, green traces) and gradient transitions (G, blue traces). A) Polymer gradients were formed with two monomers bearing a difference in density: *N*,*N*-dimethylacrylamide (0.96 g mL^{-1}) and lauryl methacrylate (0.87 g mL^{-1}). The transition could be visualized using Rhodamine B dye (red), which was soluble only in the latter monomer. Raman spectroscopy was used to show differences in the intrinsic chemical composition profile along the longitudinal coordinate of an undyed system. Confocal Raman imaging was used to detect the ratio of CH_2 and CH_3 stretching features, demonstrating the different profiles obtained for polymers cast with a gradient or sharp transition. B) Gradients were formed with two different concentrations of gellan gum hydrogel, which could be visualized by the addition of methylene blue dye. Spherical indentations along the longitudinal coordinate were used to calculate contact modulus profiles for the gradient and sharp transition hydrogels. Sucrose was used to create density differences between the base layer and injection phase of agarose hydrogels in order to create transitions of: C) nanoparticles including gold nanoparticles (pink), liposomes labeled with Rhodamine B (red) and RFP-extracellular vesicles (orange) as well as D) 200 kDa FITC-dextran (green) and E) avidin labeled with Texas Red (yellow). Intensity profiles along the longitudinal coordinate were used to characterize the hydrogels bearing a gradient or a sharp transition. Scale bars = 1 mm. All profile plots show normalized transitions along the longitudinal coordinate, with equivalent axes scales used for each pair of graphs. For fabrication detail please refer to Table S1 in the Supporting Information.

nano-particles. For this study, we used our established agarose–sucrose system to generate gradients of gold nanoparticles, 1-palmitoyl-2-oleoyl-glycero-3-phosphocholine (POPC) liposomes, and cell-derived extracellular vesicles (Figure 2C). These three examples encompassed a broad range of inorganic, organic, and biological nanoparticles, each of which can be used as a host for cargo delivery or as a functional entity in its own right.[13,21–23] We next investigated whether our buoyancy platform could support the formation of biomolecular gradients. Again using our agarose–sucrose system, we patterned gradients of both macromolecules (fluorescently tagged 200 kDa dextran) and proteins (fluorescently tagged avidin) (Figure 2D). It should be noted, however, that due to the absence of any strong attractive interactions with the agarose network, the avidin and dextran were only temporarily entrapped within the hydrogel (Figure S6, Supporting Information). To establish a more prolonged gradient, we investigated whether we could pattern cargo associated with a macromolecular host that was covalently crosslinked to the surrounding hydrogel network. We demonstrated this concept using gelatin methacryloyl (GelMA) as the bulk hydrogel and heparin methacryloyl (HepMA) as a macromolecular host. While heparin has been widely used to sequester cationic proteins,[24,25] the addition of methacryloyl groups provided a means to covalently crosslink HepMA with itself and the surrounding GelMA. Indeed, this approach limited the cumulative release of HepMA from GelMA to just 26 ± 3% after 28 d of incubation, compared to an 86 ± 16% release of unmodified heparin from GelMA after just 1 d of incubation (Figure S7, Supporting Information). To demonstrate the cargo-loading capability, we used fluorescently tagged avidin (M_W = 66 kDa, pI = 6.5, heparin dissociation constant = 160×10^{-9} M) as a model protein.[26] By coinjecting 10% (w/v) GelMA and avidin sequestered with HepMA into a base layer of 10% (w/v) GelMA with 5% (w/v) sucrose, we successfully generated well-defined protein gradients (Figure 2E). It is important to note that orthogonal methacrylate chemistry was chosen in order to bind HepMA and GelMA without forming covalent linkages with the protein cargo. Consequently, this approach reduces the chance of denaturation while retaining the possibility for slow cargo release.

The ability of our buoyancy platform to rapidly cast biomaterial gradients offers great potential for the engineering of complex tissue structures. For instance, a major challenge of regenerative medicine is the engineering of the osteochondral interface that exists between cartilage and bone. In nature, this transition arises, in part, by an anisotropic distribution of growth factors present during the process of endochondral ossification.[27] Accordingly, we sought to use our buoyancy platform to present a gradient distribution of BMP-2, a key developmental growth factor that can be used to initiate osteogenesis in human mesenchymal stem cells (hMSCs).[28] Given that BMP-2 is a low molecular weight cationic protein (M_W = 13 kDa, pI = 8.5, heparin dissociation constant = 20×10^{-9} M),[29] we elected to use HepMA as a macromolecular host patterned within a GelMA hydrogel (similar to our previous example using avidin). As a bulk material, GelMA has been used extensively to support hMSCs during cartilage, bone and osteochondral tissue engineering,[30] while heparin has been used to electrostatically bind and slowly release functionally active BMP-2.[31] To test this behavior, we used an enzyme-linked immunosorbent assay to measure the cumulative release of BMP-2 from homogeneous HepMA–GelMA hydrogels (Figure S8, Supporting Information). We observed a slow release that reached completion at 28 d of incubation, which should ensure that BMP-2 is elevated at one end of the hydrogel throughout the culture period.

The only aspect of the HepMA–GelMA system that was not suitable for tissue engineering was the density modifier: although sucrose is ideal for fabricating gradients in cell-free systems, it is known to exert an osmotic pressure that can be highly cytotoxic. Accordingly, we investigated whether we could substitute sucrose for the more cytocompatible polysaccharide Ficoll in order to raise the density of GelMA in the base layer while maintaining a stable osmotic pressure. Indeed, an alamarBlue assay confirmed that doping up to 5% (w/v) Ficoll in GelMA hydrogels presented no significant cytotoxicity to the encapsulated hMSCs (Figure S9A, Supporting Information). Crucially, Ficoll could be used in the same way as sucrose to produce gradients in GelMA with a longitudinal profile that was dependent upon injection rate (Figure S9B, Supporting Information). Thus, our optimized system for osteochondral tissue engineering comprised 3.1 µg mL^{-1} BMP-2, 2.5 µg mL^{-1} HepMA and 10% (w/v) GelMA injected into a base layer of 10% (w/v) GelMA doped with 5% (w/v) Ficoll, with both phases containing 9×10^6 hMSCs mL^{-1} and 2.5 mg mL^{-1} photoinitiator. Using these conditions, and an injection rate of 17 µL s^{-1}, we were able to establish smooth gradients of HepMA and BMP-2 that could be immobilized in GelMA using UV light irradiation (5 min, 365 nm, 6 mW cm^{-2}) (**Figure 3**A). We used these constructs for a 28 d course of osteochondral tissue engineering using a defined osteochondral differentiation medium that we have previously shown to be capable of supporting both osteogenesis and chondrogenesis (Figure 3A).[13] This medium included 2×10^{-3} M β-glycerophosphate as a phosphate source,[32] transforming growth factor β3 (TGF-β3) to stimulate chondrogenesis, alongside supporting components such as insulin–transferrin–selenium, ascorbic acid, and dexamethasone.

We started to observe the formation of a strikingly opaque cap on the cultured constructs after approximately 15 d of tissue engineering. By the end of the culture period (28 d), this cap was present on all tissue constructs, a strong indication that the BMP-2 gradient had guided a localized mineralization process. Indeed, when we examined sections of osteochondral tissue using Alizarin Red S staining, we observed a mineralized cap exclusively at one end of the tissue (Figure 3B). On the other hand, Alcian Blue staining revealed that the entire tissue contained sulfated glycosaminoglycans, a key extracellular matrix component naturally present in both cartilage and bone (Figure 3C).[33] These findings were corroborated using immunofluorescence staining for key proteins associated with chondrogenesis and osteogenesis (Figure 3D,E). While type II collagen, found exclusively in hyaline cartilage,[34] was present throughout the tissue construct, osteopontin, a key marker of osteogenesis, was observed only in the mineralized cap.[35] We further investigated the mineral composition and distribution using Raman spectroscopic imaging, which revealed the presence of both hydroxyapatite (HAP) and β-tricalcium phosphate (β-TCP), exclusively at the bone end of the construct

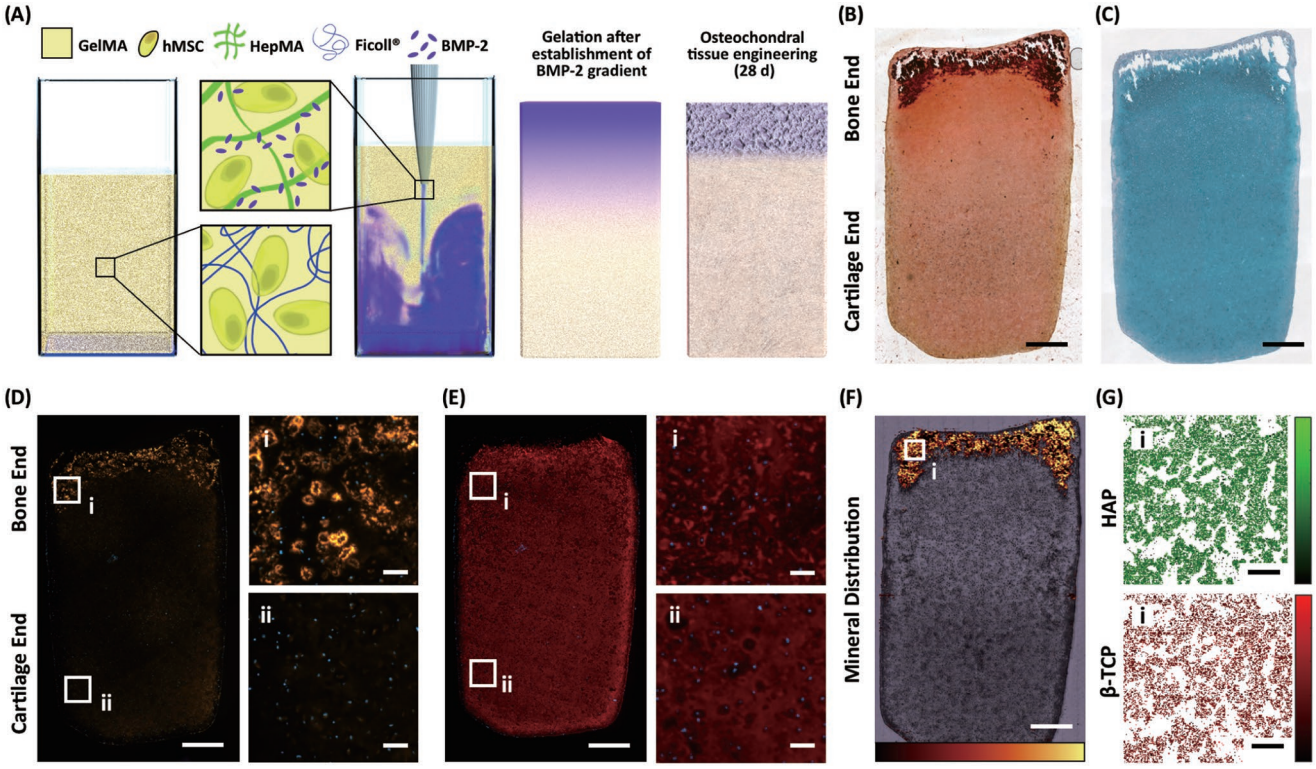

Figure 3. Growth factor gradients for osteochondral tissue engineering. A) BMP-2 was sequestered by HepMA and coinjected with 10% (w/v) GelMA and hMSCs into a base layer of 10% (w/v) GelMA, 5% (w/v) Ficoll and hMSCs. The GelMA and HepMA were photo-crosslinked to preserve the BMP-2 gradient in a self-supporting hydrogel, which was cultured for 28 d in osteochondral differentiation medium. Note that the components in the inset images are not drawn to scale. Histology and immunofluorescence staining confirmed the formation of osteochondral tissue: B) Alizarin Red S staining revealed localized mineral deposition at one end of the tissue; C) Alcian Blue staining revealed tissue-wide staining for glycosaminoglycans, a component of both cartilage and bone; D) the bone-specific marker osteopontin was also localized exclusively at the mineralized cap; E) Type II collagen, a component of hyaline cartilage, was present throughout the tissue. F) Raman spectroscopic imaging was used to reveal the spatial distribution of mineral and G) identify the presence and heterogeneous presentation of both hydroxyapatite and tri-calcium phosphate in the mineralized cap. Scale bar = 1 mm in low-magnification images, 100 µm in high magnification images. The color scales in (F) and (G) show the relative intensity of signal, with brighter color representing higher intensity.

(Figure 3F,G). While the HAP signature was stronger throughout the mineral cap region, spectral unmixing of these features indicated a heterogeneous presentation of mineral species that formed colocally within the cultured construct. Taken together, the histology, immunofluorescence staining and Raman spectroscopic mapping strongly suggested that the soluble TGF-β3 had stimulated tissue-wide chondrogenesis of the hMSCs, while the BMP-2 released from the HepMA gradient had initiated a localized osteogenic response. Interestingly, the mineralization took the form of an abrupt biphasic transition between bone and cartilage, despite the initially smooth BMP-2 gradient and the homogenous distribution of cells (Figure S10, Supporting Information). This observation mimics the natural process of endochondral ossification, in which concentration gradients of osteoinductive factors (e.g., BMP-2 and BMP-6) produce a sharp transition at the osteochondral interface. This transition, known as a tidemark, separates subchondral bone and calcified cartilage from the other cartilage zones and is a hallmark feature of the osteochondral interface. Interestingly, we have observed a similar phenomenon in previous osteochondral tissue engineering systems[13] and hypothesize that a threshold level of BMP-2 may be required to initiate and sustain mineralization, which could in turn produce a positive feedback loop whereby the deposited mineral acts to further stimulate osteogenesis. Further work is required to test this theory, which could shed light upon some of the key developmental processes that occur during endochondral ossification.

In conclusion, we have introduced a versatile platform that uses the fundamental force of buoyancy to pattern materials with tunable gradients using one simple injection event. We demonstrated gradient formation with a range of different materials (polymers and hydrogels) and cargos (liposomes, inorganic nanoparticles, extracellular vesicles, macromolecules, and small molecules). We also demonstrated the applicability of this platform in a tissue engineering context, specifically, the presentation of a BMP-2 gradient for the production of osteochondral tissue. The resulting tissue constructs possessed distinct regions of bone and cartilage, along with a structural transition that resembled the tidemark observed at the native osteochondral interface. Overall, the versatility, speed, and ease of use of our platform technology offer the opportunity for many different applications in gradient material fabrication and interfacial tissue engineering.

Experimental Section

Buoyancy-Driven Gradient Casting and Characterization: Unless stated otherwise, all chemicals used were from Sigma Aldrich. To create the gradient constructs, the denser liquid was added to a mold as a base layer. An electronic dispenser (Multipette E3/E3x, Eppendorf) was used to inject the lighter liquid at a defined flow rate, with the injection outlet maintained at the liquid–air interface of the base layer. Injection rates were measured manually. Immediately after injection, the dispenser was removed, and the gradients were preserved by gelation or polymerization. Two molds were used in this communication: a cuboid mold ($5 \times 15 \times 3$ mm) and a cylindrical mold ($\varnothing = 5$ mm, $h = 15$ mm). Polymer gradients were characterized using Raman spectroscopic mapping. Briefly, a confocal Raman microspectroscopy system (WITec alpha 300R+) was used to raster map the entire surface of the gradient construct and obtain spectra comprising compositional information at 50 µm steps.[36,37] The resulting data was analyzed via peak ratio to reveal the location and relative concentration of the construct polymers. Stiffness gradients were characterized using spherical indentation mapping. Briefly, a 3 mm diameter stainless steel sphere was indented along the gradient in 0.5 mm steps, and the contact modulus of each indent was characterized by a modified Hertzian solution to account for substrate effects.[38] All other gradients were characterized by imaging the constructs using a wide field microscope, converting the images to 16-bit and then using the plot profile function in Image J. For full details of the fabrication and characterization of each gradient system, see Table S1 and the Experimental Section in the Supporting Information.

Osteochondral Tissue Engineering: hMSCs (Lonza) were cultured with MesenPro RS medium (Thermo Fisher Scientific) and used between passage 4–5. For osteochondral tissue engineering, we used a 90 µL base layer of 5% (w/v) Ficoll-400, 10% (w/v) GelMA, 2.5 mg mL^{-1} Irgacure 2959, and 9×10^6 hMSCs mL^{-1} and a 45 µL injection phase of 12.5 µg mL^{-1} BMP-2 (R&D Systems), 10 µg mL^{-1} HepMA, 10% (w/v) GelMA, 2.5 mg mL^{-1} Irgacure 2959 and 9×10^6 hMSCs mL^{-1}. Note that prior to gradient formation, HepMA and BMP-2 were mixed for at least 4 h to ensure equilibration. We used an injection rate of 16.7 µL s^{-1} and then used a UV lamp to crosslink the hydrogels (365 nm, 6 mW cm^{-2}, 5 min), which were then transferred to a 24 well plate. The constructs were cultured in osteochondral differentiation medium, which was changed three times a week. The osteochondral differentiation medium comprised high glucose Dulbecco's modified Eagle medium with pyruvate (Thermo Fisher Scientific), 1× insulin–transferrin–selenium supplement (ITS+, BD), 100×10^{-9} M dexamethasone, 50 µg mL^{-1} L-ascorbic acid, 50 µg mL^{-1} L-proline, 2×10^{-3} M β-glycerophosphate and 10 ng mL^{-1} TGF-β3 (R&D Systems). After 28 d of culture, the constructs were harvested and characterized using histology (Alcian Blue, Alizarin Red), immunofluorescence staining (type II collagen, osteopontin) and Raman spectroscopy. For full details of the tissue engineering and analysis, please refer to the Materials and Methods section in the Supporting Information.

Supporting Information

Supporting Information is available from the Wiley Online Library or from the author.

Acknowledgements

C.L. was supported by a Top University Strategic Alliance Ph.D. Scholarship from Taiwan. L.O. acknowledges support from the Engineering and Physical Sciences Research Council (EPSRC) Programme Grant "Engineering growth factor microenvironments—a new therapeutic paradigm for regenerative medicine" (EP/P001114/1). I.J.P. and A.C.M. acknowledge support from the Whitaker International Program, Institute of International Education, USA. C.W.W. acknowledges support from the Biotechnology and Biological Sciences Research Council Doctoral Training Partnership (BB/N503952/1). J.P.K.A. acknowledges support from the Arthritis Research U.K. Foundation (21138) and the Medical Research Council (MRC) (MR/S00551X/1). M.M.S. and Y.L. acknowledge support from the European Research Council Seventh Framework Programme Consolidator grant "Naturale CG" (616417). M.M.S. acknowledges support from the grant from the UK Regenerative Medicine Platform "Acellular/Smart Materials—3D Architecture" (MR/R015651/1) and the Wellcome Trust Senior Investigator Award (098411/Z/12/Z). We thank the Facility for Imaging by Light Microscopy (FILM) at Imperial College London, and acknowledge the assistance provided by Dr. Vincent Leonardo in producing the fluorescent cell line used to generate extracellular vesicles, Dr. Yunqing Zhu for advice in polymer experiments, and Dr. John Goertz for assistance with graphic design in Figures 1 and 3. Raw data are available online at https://doi.org/10.5281/zenodo.2578001. C.L. conceived the project and carried out the majority of experimental work; C.L. and L.O. performed the tissue engineering experiments; I.J.P. performed all Raman spectroscopy experiments; A.C.M. performed all mechanical characterization; Y.L. and L.O. assisted on the material modification and synthesis; C.W.W. assisted with extracellular vesicle production; J.P.K.A. and M.M.S. supervised the work; and C.L., J.P.K.A., and L.O. wrote the paper with contributions from all authors.

Conflict of Interest

The authors declare no conflict of interest.

Keywords

biomaterials, buoyancy, gradients, osteochondral, tissue engineering

Received: January 14, 2019
Revised: February 18, 2019
Published online: March 7, 2019

[1] H. H. Lu, S. Thomopoulos, *Annu. Rev. Biomed. Eng.* **2013**, *15*, 201.
[2] P. B. Messersmith, *Science* **2008**, *319*, 1767.
[3] F. Ulloa, J. Briscoe, *Cell Cycle* **2007**, *6*, 2640.
[4] P. Garrison, S. Yue, J. Hanson, J. Baron, J. C. Lui, *PLoS One* **2017**, *12*, e0176752.
[5] J. L. Christian, *Wiley Interdisp. Rev.: Dev. Biol.* **2012**, *1*, 3.
[6] V. Vogel, M. Sheetz, *Nat. Rev. Mol. Cell Biol.* **2006**, *7*, 265.
[7] H. L. Ashe, J. Briscoe, *Development* **2006**, *133*, 385.
[8] M. Singh, C. Berkland, M. S. Detamore, *Tissue Eng., Part B* **2008**, *14*, 341.
[9] J. Shi, L. Wang, F. Zhang, H. Li, L. Lei, L. Liu, Y. Chen, *ACS Appl. Mater. Interfaces* **2010**, *2*, 1025.
[10] X. Zhang, X. Gao, L. Jiang, J. Qin, *Langmuir* **2012**, *28*, 10026.
[11] L. G. Bracaglia, B. T. Smith, E. Watson, N. Arumugasaamy, A. G. Mikos, J. P. Fisher, *Acta Biomater.* **2017**, *56*, 3.
[12] K. A. Mosiewicz, L. Kolb, A. J. van der Vlies, M. M. Martino, P. S. Lienemann, J. A. Hubbell, M. Ehrbar, M. P. Lutolf, *Nat. Mater.* **2013**, *12*, 1072.
[13] C. Li, J. P. K. Armstrong, I. J. Pence, W. Kit-Anan, J. L. Puetzer, S. Correia Carreira, A. C. Moore, M. M. Stevens, *Biomaterials* **2018**, *176*, 24.
[14] J. S. Turner, *J. Fluid Mech.* **1966**, *26*, 779.
[15] A. Boyum, *Scand. J. Clin. Lab. Invest., Suppl.* **1968**, *97*, 77.
[16] R. J. Britten, R. B. Roberts, *Science* **1960**, *131*, 32.

[17] L. Bai, X. Ma, J. Liu, X. Sun, D. Zhao, D. G. Evans, *J. Am. Chem. Soc.* **2010**, *132*, 2333.
[18] V. Parameswaran, A. Shukla, *J. Mater. Sci.* **2000**, *35*, 21.
[19] J. T. Beals, M. S. Thompson, *J. Mater. Sci.* **1997**, *32*, 3595.
[20] A. Di Luca, C. Van Blitterswijk, L. Moroni, *Birth Defects Res., Part C* **2015**, *105*, 34.
[21] J. P. K. Armstrong, M. M. Stevens, *Adv. Drug Delivery Rev.* **2018**, *130*, 12.
[22] T. M. Allen, P. R. Cullis, *Adv. Drug Delivery Rev.* **2013**, *65*, 36.
[23] P. Ghosh, G. Han, M. De, C. K. Kim, V. M. Rotello, *Adv. Drug Delivery Rev.* **2008**, *60*, 1307.
[24] Y. I. Chung, K. M. Ahn, S. H. Jeon, S. Y. Lee, J. H. Lee, G. Tae, *J. Controlled Release* **2007**, *121*, 91.
[25] S. A. Abbah, J. Liu, R. W. Lam, J. C. Goh, H. K. Wong, *J. Controlled Release* **2012**, *162*, 364.
[26] W. C. Kett, R. I. Osmond, L. Moe, S. E. Skett, B. F. Kinnear, D. R. Coombe, *Biochim. Biophys. Acta, Gen. Subj.* **2003**, *1620*, 225.
[27] F. Las Heras, H. K. Gahunia, K. P. Pritzker, *Orthop. Clin. North Am.* **2012**, *43*, 155.
[28] D. Noel, D. Gazit, C. Bouquet, F. Apparailly, C. Bony, P. Plence, V. Millet, G. Turgeman, M. Perricaudet, J. Sany, C. Jorgensen, *Stem Cells* **2004**, *22*, 74.
[29] R. Ruppert, E. Hoffmann, W. Sebald, *Eur. J. Biochem.* **1996**, *237*, 295.
[30] J. Yang, Y. S. Zhang, K. Yue, A. Khademhosseini, *Acta Biomater.* **2017**, *57*, 1.
[31] B. Zhao, T. Katagiri, H. Toyoda, T. Takada, T. Yanai, T. Fukuda, U. I. Chung, T. Koike, K. Takaoka, R. Kamijo, *J. Biol. Chem.* **2006**, *281*, 23246.
[32] J. Hwang, E. M. Kyubwa, W. C. Bae, W. D. Bugbee, K. Masuda, R. L. Sah, *Cartilage* **2010**, *1*, 287.
[33] V. M. Mania, A. G. Kallivokas, C. Malavaki, A. P. Asimakopoulou, J. Kanakis, A. D. Theocharis, G. Klironomos, G. Gatzounis, A. Mouzaki, E. Panagiotopoulos, N. K. Karamanos, *IUBMB Life* **2009**, *61*, 447.
[34] E. H. Morrison, M. W. Ferguson, M. T. Bayliss, C. W. Archer, *J. Anat.* **1996**, *189*, 9.
[35] J. Sodek, B. Ganss, M. D. McKee, *Crit. Rev. Oral Biol. Med.* **2000**, *11*, 279.
[36] E. Butchert, T. R. Manley, *Spectrochim. Acta, Part A* **1978**, *34*, 781.
[37] H. Edwards, A. Johnson, E. E. Lawson, *Spectrochim. Acta, Part A* **1994**, *50*, 255.
[38] A. C. Moore, J. F. DeLucca, D. M. Elliott, D. L. Burris, *J. Tribol.* **2016**, *138*, 041405.